Facile decoration of carbon fibers with Ag nanoparticles for adsorption and photocatalytic reduction of CO_2

Jie Ding [a,b], Yunfei Bu [a,c], Man Ou [a,c], Yang Yu [a,c], Qin Zhong [a,c,*], Maohong Fan [b,**]

[a] School of Chemical Engineering, Nanjing University of Science and Technology, Nanjing, Jiangsu 210094, PR China
[b] Department of Chemical and Petroleum Engineering, University of Wyoming, Laramie, WY 82071, USA
[c] Nanjing AIREP Environmental Protection Technology Co., Ltd., Nanjing, Jiangsu 210091, PR China

ARTICLE INFO

ABSTRACT

Carbon fibers (CFs) decorated with Ag nanoparticles (Ag NPs), hereafter denoted as Ag NPs/CFs, have been successfully synthesized via a simple solution dipping combined with an ultrasonic treatment. CFs are decorated by spherical Ag NPs with 20–50 nm diameters mainly consisted of the Ag nanocrystals, which is reduced from Ag^+ by both CFs and polyviylpyrrolidone (PVP). The aggregation of Ag NPs on the surface of CFs via Ostwald ripening and from the solution are the primarily responsible for the formation of spherical Ag NPs. The as-prepared Ag NPs/CFs Exhibits 4-time higher of photocatalytic activity than the pure Ag NPs, meanwhile enhancing the selectivity to convert CO_2 into CH_3OH. A possible visible light photocatalytic mechanism for the better performance and selectivity of Ag NPs/CFs is discussed. The significant enhancement of the CO_2 photocatalytic reduction is primarily attributed to the increase of CO_2 adsorption and the efficient electron transfer to CO_2 as well as the active site splitting of CO_2 reduction and H_2O decomposition.

© 2016 Published by Elsevier B.V.

1. Introduction

Due to the excessive dependence on fossil resources, global warming and increasing CO_2 emission in the atmosphere are the severe problems faced worldwide. Conversion of CO_2 into clean fuels and energy-rich chemicals could be one of the most efficient solutions to these problems [1,2]. Toward this goal, biomimetic artificial photosynthesis has recently gained much attention as a promising technology for reduction of CO_2 to energy-rich chemicals using solar energy. In this process, the hydrocarbons are produced from photoreduction of CO_2 using H_2O and solar energy [3,4]. In 1979, Inoue et al. firstly illustrated the photocataytic reduction of CO_2 to form organic compounds by using a photosensitive semiconductor [5]. Afterwards, various photocatalytic systems involving transition-metal or metal complexes have been explored toward the photocatalytic CO_2 reduction, but most of them were efficient only with the presences of organic solvents or water-organic solvents as sacrificial reductant [6,7]. The photocatalytic systems using

H_2O as the reductant for CO_2 reduction still need to be developed. Extensively researchers started with the semiconductors such as TiO_2 or TiO_2-based heterogeneous photocatalysts due to their low cost and high chemical stability [8]. However, the flat-band potential of electrons in the conduction band of these semicondutors is lower than that required for CO_2 photoreduction, thus resulting in low efficiency [9]. Therefore, metal catalysts like Au, Ag and Pt series type photocatalysts for CO_2 reduction have gradually attracted attention not only due to their efficiently surface Plasmon resonance under visible light but also stably photocatalytic activity in the whole solar spectral region [10,11]. Unfortunately, most of these catalysts still exhibit low catalytic activity or selectivity for CO_2 reduction because of the easy recombination of their Plasmon-induced electron-hole pairs generated by the electron excitations from HOMO to LOMO [12,13]. Previous studies have reported that the acceleration of electron transfer to CO_2 benefited the separation of electron-hole pairs [14–16]. Therefore, large amounts of efforts have been made to improve the electron transfer in recent years. For example, Lim et al. embedded S or As into the Ag based catalysts to improve the free electron transfer and minimize the overpotential, resulting in the significant promotion of CO_2 photoreduction [14]. Yang et al. prepared the Ag/Pt clusters loaded on TiO_2 (101) or Ag clusters loaded on Ga_2O_3 to improve the enhancement of CO_2 photoreduction through the facilitation of the electron transfer from catalysts to CO_2 [15]. Cheng et al. utilized Pt to modify

the reduced graphene oxide for improving the electron transfer of Pt, thus apparently enhancing the photocatalytic reduction of CO_2 [16]. However, besides the electron transfer, the adsorption of CO_2 may be also one of the important factors for photocatalytic CO_2 reduction. In previous papers, carbon fibers (CFs) have been harnessed recently in optical, electronic, and catalytic devices because of their well electron conductivity [17,18]. The CFs has been confirmed to obtain well CO_2 adsorption in the present study. Importantly, they have low price and can be prepared under simple processes. Therefore, it will be interesting and valuable to explore the possible promotional effect of CFs on photocatalytic reduction of CO_2.

In the present study, CFs decorated with Ag nanoparticles (Ag NPs), denoted as Ag NPs/CFs, were firstly used as the possibly efficient catalyst for CO_2 reduction with H_2O as the reducing agent. Compared to other noble metals, Ag not only has much lower price, but also can produce hot electrons through the surface Plasmon resonance of Ag NPs, and these hot electrons are easily injected into the conductors or the conduction band of semiconductors [19,20]. Additionally, such properties of surface Plasmon resonance of noble metal nanoparticles including Ag NPs have been widely applied in the water splitting due to their strong reactivity with H_2O [21,22]. The hot electrons excited by surface Plasmon resonance of Ag NPs are injected into the CFs possessing high conductivity, efficiently increasing the electron transfer and thus the separation of electron-hole pairs. Similar electron transfer from the noble metal nanoparticles to the higher conductive materials for improving the separation of electron-hole pairs has been reported previously [23,24]. Moreover, the nanoscale CFs benefit to the well dispersion of Ag NPs for enhancing light absorption and reaction with H_2O. The electrons transferred from Ag NPs to CFs are helpful to the electron obtaining of adsorbed CO_2 on the surface of CFs. Therefore, it is expected that Ag NPs/CFs potentially provide novel and well photocatalysis for CO_2 reduction. Hence, the development of Ag NPs/CFs system is of fundamental and practical significance.

Herein, a facile method for growing spherical Ag NPs on CFs is developed by solution dipping combined with ultrasonic method. The formation mechanisms of such catalysts have been proposed. The obtained Ag NPs/CFs has been utilized for high-efficiency photocatalytic reduction of CO_2. The promotional mechanisms for CO_2 reduction with Ag NPs/CFs as the photocatalyst have been discussed.

2. Experimental sections

2.1. Ag NPs/CFs photocatalyst preparations

CFs was prepared through a simple electrospinning method. In brief, polyvinylpyrolidone (PVP, M_W = 360,000 g/mol, Sigma Aldrich) and Polyacrylonitrile (PAN, MW = 1,500,000 g/mol, Sigma Aldrich) were dissolved into *N,N*-dimethylformamide (DMF, 10 mL, Sinopharm Chemical Reagent Co., Ltd.) with vigorous stirring for 24 h to form a 10 wt% solution. The electrospun was conducted in a homemade setup as shown in Fig. 1a. The resulting solutions were sprayed from stainless-steel needle to the rotating collector screen. The applied voltage was fixed at 18 kV and the distance from the needle to the collector was maintained at 15 cm. After drying and calcinations at 1000 °C for 2 h in the N_2 atmosphere, the final products CFs were obtained.

Silver nitrate (AgNO₃, purity 99.8%, AR, Sinopharm Chemical Reagent Co., Ltd.) was used as the precursor in the preparation of the Ag NPs, and polyvinylpyrrolidone (PVP, M_W = 40,000, Sigma Aldrich) served as the stabilizer. An aqueous solution of silver nitrate (0.2 M, 50 mL) was prepared, and 200 mg of the CFs were immerged into the solutions to be ultrasonically treated for 5 h 5 wt% of PVP aqueous solution was slowly added into the aqueous AgNO₃ solutions with immerging CFs during ultrasonic treatment.
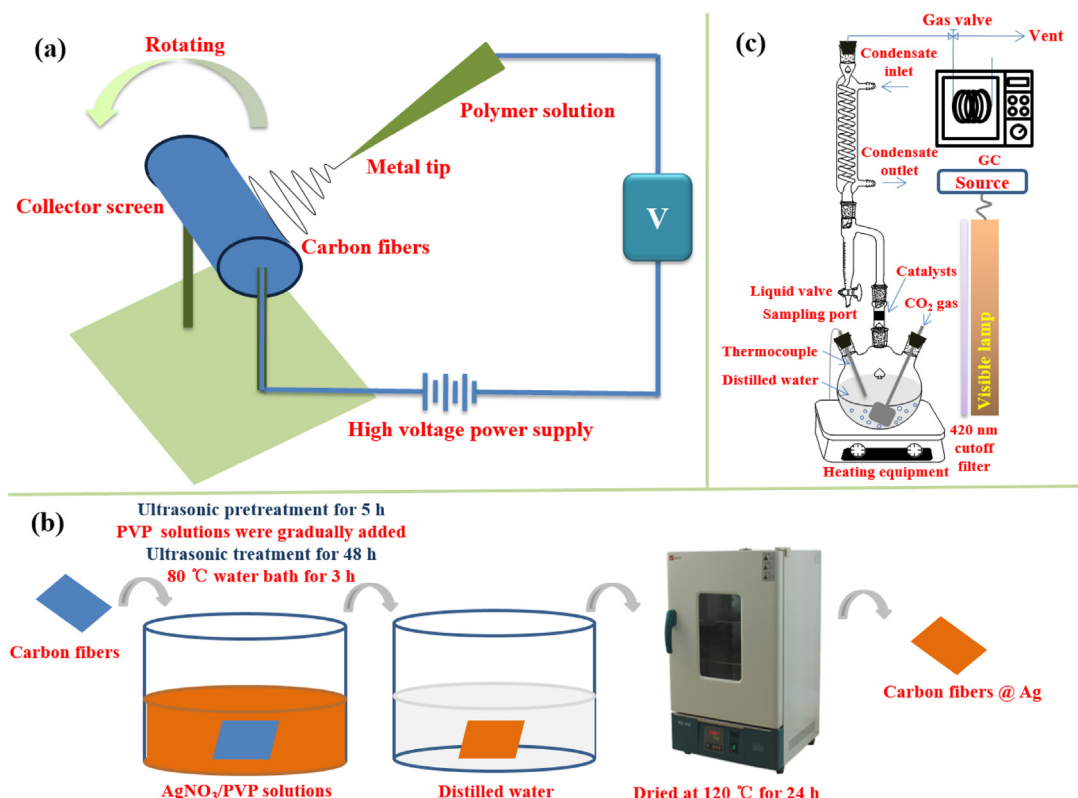

Fig. 1. Schematic of (a) electrospun, (b) process of catalyst preparation and (c) photocatalytic test equipment.

The above mixed solution continues to be ultrasonically treated for 48 h. After ultrasonic treatment, the solution was heated in 80 °C with water bath for 3 h. The color of the solution changed to dark brown due to the reduction of Ag^+ to Ag^0. At the end of the reactions, the CFs were washed with distilled water, and then dried at 120 °C in the atmosphere of air for 24 h. The preparation process was illustrated in Fig. 1b.

2.2. Characterizations of catalysts

The powder X-ray diffraction (XRD) measurement was carried out with Beijing Purkinjie general instrument XD-3 X-ray diffraction (CuKα, voltage 35 kV, electrical current 20 mA, 2θ from 5° to 80°). The Fourier Transform Infrared Spectroscopy (FTIR) was recorded on an IS10 spectrometer (Nicolet, USA). X-ray photoelectron spectroscopy (XPS) experiments were carried out on a RBD upgraded PHI-5000C ESCA system (Perkin Elmer) with Mg Kα radiation (hν = 1253.6 eV), calibrated by the C 1s peak at 284.6 eV with an accuracy of 0.1 eV. Photoluminescence (PL) spectra at room temperature using a Labram-HR800-type spectrophotometer (Jobin Yvon Co., France) with a He-Cd laser (λ = 325 nm) as the light source. Microstructures of the catalyst were observed by scanning electron micrograph (SEM) in Philips XL-30 (Holland) system at a voltage of 15 kV. The EDX was performed by an Energy Dispersive X-Ray Spectra in Thermo Scientific Kevex UltraDry (USA). Transmission electron microscope (TEM) observations were carried out using a Philips CM-10 at 80 kV and a CM-12 at 120 kV. The UV–vis diffuse reflectance spectra (DRS) were performed on a Shimadzu UV-2550 UV–vis spectrophotometer using $BaSO_4$ as the reference sample. Electrochemical impedance spectra (EIS) were performed on a VersaSTAT3 electrochemical workstation (Parstat, USA) ranging the frequency from 825 kHz to 0.1 Hz with 5 mV amplitude perturbation. The electrolyte is 0.5 mol/L Na_2SO_4, and the electrode is the glassy carbon. The products from photocatalytic reduction of CO_2 were identified with an Aglient 7890A/5975C gas chromatography-mass spectrometer (GC–MS). The isotope experiment were conducted according to the reported method with modification [25]. The resulted solutions were heated to 80 °C under the purge of N_2. The exhausted gas was introduced into the tetrahydrofuran. After 5 h, the obtained tetrahydrofuran was tested by GC–MS.

2.3. Photocatalytic activity tests

The photocatalytic reduction of CO_2 was performed in a 20 mL homemade reactor at ambient temperature and atmospheric pressure (Fig. 1c). The reactor has six parts: the light system, the 420 nm cutoff filter, the H_2O vapor generation system, the fixed bed reactor, the vapor condensation system, and the heating system. Typically, 10 mg catalysts were paved or spread and fixed onto the fixed bed. The liquid valve was shut down, and the gas valve was connected to the vent. Before irradiation, the reactor was blown with CO_2 for 30 min to remove air and ensure that the reaction system was under anaerobic conditions. When irradiation, the CO_2 with a 20 mL·min^{-1} flow rate was introduced into the H_2O with aeration head in distilled H_2O storage flask. The heating system kept the temperature at 80 °C. The H_2O vapor and CO_2 together passed through the catalysts. Some of water was condensed and back flowed into the H_2O storage flask. Others were entered into the vapor condensation system, and the condensate products flowed to the bottom. The sample in the bottom was collected and analyzed by GC. The vapor condensation system was cooled by the water. The exhausted gas was introduced into the GC (SP-1000, Beifen, China) with a flame ionized detector (FID) and a HP-5 column. A 350 W Xe lamp was used as the light source. 1 μL of liquid products was taken from the bottom every 1 h irradiation and analyzed by gas chromatograph

(GC-9860, Shangfen, China) equipped with a flame ionized detector (FID) and a porapak Q column. Products were calibrated with a standard mixture and determined by the retention time. Nitrogen of high purity (≥99.999) was used in GC-9860 as carrier gas.

3. Results and discussions

3.1. Structural characterizations

The morphologies of the samples are observed by SEM. As shown in Fig. 2a and b, the CFs show smoothly fibrillar in shape with diameters of around 200 nm. On the contrary, Fig. 2c and d shows that the Ag NPs/CFs display rough surface morphologies and amounts of spherical nanoparticles with diameters of 20–50 nm are well dispersed onto the CFs. The composition of the Ag NPs/CFs was determined with energy dispersive X-ray spectroscopy (EDX) (Fig. 2e–h). Fig. 2e and g give the location of EDX on Ag NPs/CFs, and Fig. 2f and h present the results of EDX of the location on Ag NPs/CFs shown in Fig. 2e and g, respectively. The results indicate that the spherical nanoparticles are only consisted of Ag without any other elements (The Au observed is derived from the pretreatment of Au spraying and not included in the table), while the elements on the surface of CFs are mainly composed of carbon and oxygen without Ag. The spherical nanoparticles are possibly formed through the aggregation of Ag NPs on CFs. Such Ag NPs aggregation on the surface of fibers has also been previously reported [26,27]. Typically, Sanjoy et al. reported the decoration of polyaniline with Ag NPs, which were aggregated to around 20 nm irregular particles and dispersed on the surface of fibers [26]. However, well-dispersion spherical nanoparticles on the surface of CFs were firstly obtained in the present study, maybe resulted from the ultrasonic treatment combined with the possible reaction between Ag^+ and CFs.

Distribution of the functional groups upon the CFs and Ag NPs/CFs was studied by FTIR analysis (Fig. 3a). The two samples show that an intense and broad band at 3436 cm^{-1} corresponds to —OH stretching vibrations in the adsorbed H_2O by carbon samples. Intense bands at 1620 cm^{-1} and 1388 cm^{-1} are observed for the two samples, which are associated with —C=O in a six-membered ring or aromatic ring and the bending in-plane —OH vibrations of —COOH, respectively [28,29]. The broad bands present in the two spectra between 1300 cm^{-1} and 900 cm^{-1} are due to the stretching C—O vibrations [30,31]. In comparison with the CFs, the intensity of bands at 1620 cm^{-1} and 1388 cm^{-1} significantly increase, suggesting that the CFs with high reducibility reduce the Ag^+ to Ag NPs on the surface of CFs during the catalyst preparation, resulting in more —C=O and —COOH groups. The Ag^+ reduction by carbon based materials such as activated carbon or carbon nanotubes has also been observed by other papers [32,33]. In their reports, the $AgNO_3$ and carbon were used as the precursor, and the Ag NPs and surface —C=O were obtained after stirring, heating and drying, further indicating that the high reducibility of carbon based materials was enough to reduce Ag^+ to Ag NPs. The above method was similar to the one reported in this research from perspective of precursors and operation procedure. Thus, it is reasonable to produce —C=O, —COOH and Ag NPs in this study. The linkage between CFs and —C=O or —COOH is shown in Fig. S1. From the results of the above EDX and Fig. S2, the O is high all around the surface of CFs, indicating that the —C=O and —COOH were well dispersed on the surface of CFs.

The XRD patterns of Ag NPs, CFs and Ag NPs/CFs are displayed in Fig. 3b. The diffraction patterns around 2θ values of 37.7°, 44.0°, 64.4° and 77.4° corresponding to (111), (200), (220) and (311) planes of Ag crystals, respectively, are apparently observed in Ag NPs [34,35]. The broad diffraction peak appeared at 2θ = 22°, corresponding to the (002) reflection of carbon [36], was observed in

(a)

(b)

(c)

(d)

(e)

Elements	C	O
Atom %	0	0
Elements	Ag	Au
Atom %	100	-

(f)

(g)

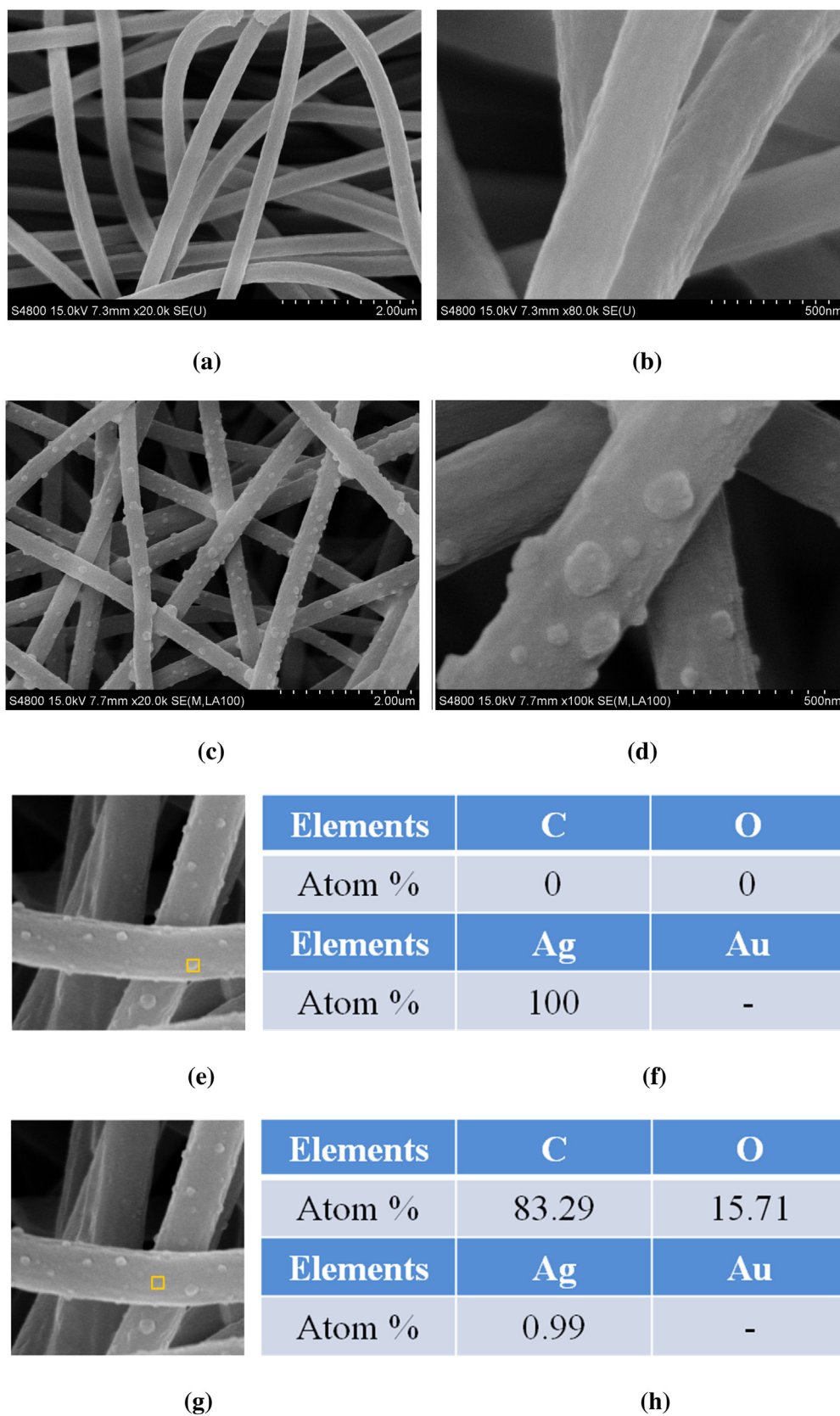| Elements	C	O
Atom %	83.29	15.71
Elements	Ag	Au
Atom %	0.99	-

(h)

Fig. 2. SEM and EDX micrographs of CFs and Ag NPs/CFs. (a,b) SEM micrographs of CFs; (c,d) SEM micrographs of Ag NPs/CFs; (e)–(h) SEM-EDX micrographs of Ag NPs/CFs.
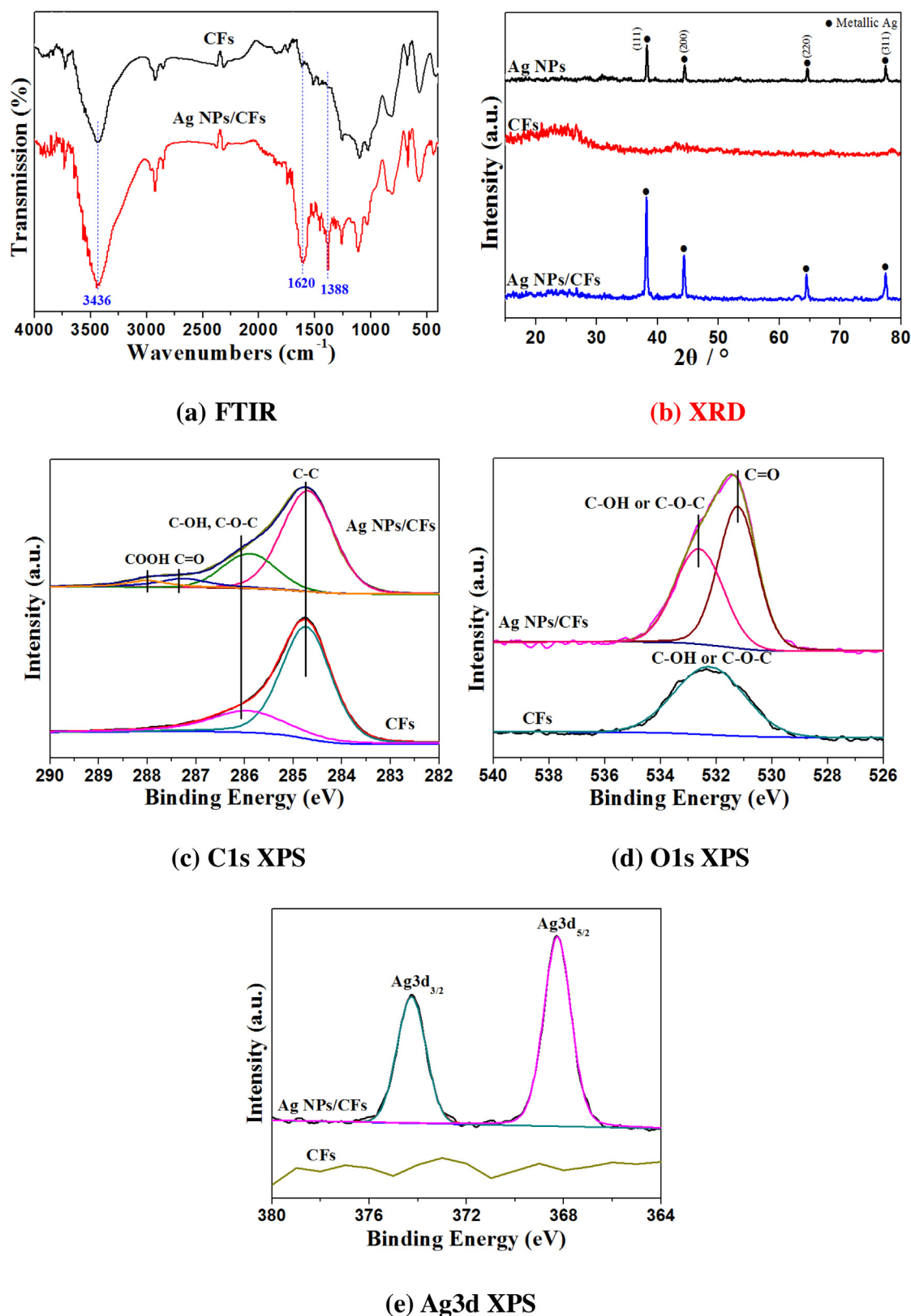
(a) FTIR

(b) XRD

(c) C1s XPS

(d) O1s XPS

(e) Ag3d XPS

Fig. 3. Structural characterizations of CF and Ag NPs/CFs. (a) FTIR spectra; (b) XRD patterns; (c)–(e) XPS spectra.

the XRD patterns of CFs. The diffraction peaks of Ag crystals are not observed for CFs, while they are clearly distinguished for Ag NPs/CFs, indicating that the Ag NPs on the surface of Ag NPs/CFs are mainly consisted of Ag nanocrystals.

As Fig. 3c–e displays, XPS analysis can provide a valuable insight into the surface structure and compositions of CFs and Ag NPs/CFs. The percentages of carbon, oxygen and silver in these two samples were calculated from C1s, O1s and Ag3d spectra and given in

Table 2
Relative area (%) of C1s peak in XPS.

Sample	C—C (284.7 eV)	C—OH, C—O—C (285.9 eV)	C=O (287.0 eV)	COOH (288.0 eV)
CFs	74.62	25.38	–	–
Ag NPs/CFs	65.18	22.14	7.83	4.85

Table 1
Composition (atomic wt.%) of CFs and Ag NPs/CFs.

Sample	C	O	O/C	Ag
CFs	95.04	4.96	0.0522	–
Ag NPs/CFs	85.50	12.82	0.1499	1.68

Table 1. The CFs contains 83.29% carbon and 4.96% oxygen, while the Ag NPs/CFs contains 85.50% carbon, 12.82% oxygen and 1.68% silver, which is slightly different from the values measured by EDX. It may be caused by two reasons. Firstly, both methods measure different areas of the Ag NPs/CFs, which may have some slight differences. Secondly, both methods may have different deviations when measuring the same samples. The increase of the oxygen content in the Ag NPs/CFs further proves the reduction of Ag^+ by CFs in the Ag NPs/CFs, leading to more polar oxygen-containing functional groups such as —C=O, —COOH on the surface of CFs. Table 2 shows the concentrations of surface functional groups presented in the CFs and Ag NPs/CFs calculated from C1s spectra, indicating the increase of the oxygen-containing functional groups like the —C=O and —COOH in Ag NPs/CFs.

As Fig. 3c shows, the C1s spectra were splitted into at most four peaks at 284.7, 285.9, 287.0 and 288.0 eV corresponding to —C—C—, —C—OH or —C—O—C—, —C=O and —COOH, respectively [37]. The CFs contains 74.62% —C—C— and 25.38% —C—OH or —C—O—C—, whereas the Ag NPs/CFs contain 65.18% —C—C—, 22.14% —C—OH or —C—O—C— and 12.68% —C=O groups. It is clear that the polar functional groups such as —C—OH, —C=O and —COOH apparently increase for Ag NPs/CFs compared to CFs. Combined with FTIR analysis, it can be obtained that the Ag^+ can be reduced to Ag NPs by CFs, which results in the oxidation of the surface of CFs.

The O1s spectra were divided into at most two peaks, as exhibited in Fig. 3d. For CFs, only one peak at 532.2 eV corresponding to —C—O can be observed, while two peaks at 531.2 eV and 532.6 eV attributed to the oxygen in —C=O and —C—O—, respectively, appear in Ag NPs/CFs [38,39]. The oxygen atoms in —COOH on the surface of Ag NPs/CFs can be presented in two peaks at 531.2 eV and 532.6 eV in O1s spectrum because oxygen atoms in —COOH groups have both single and double bonds with carbon atoms. The increase of the oxygen species for Ag NPs/CFs further suggests that the reduction of Ag^+ to Ag NPs results in the formation of numerous oxygen-containing functional groups. It has been reported that the Ag^+ generated from aqueous $AgNO_3$ solution was first stably anchored on the —OH groups of the carbon surface via the ion-dipole interaction due to its high affinity toward oxygen [40,41]. And then the Ag^+ on the surface was further reduced by the —OH groups or the reducer in the solution. As demonstrated in O1s and C1s spectra, the content of —OH groups on the surface of CFs only slightly decreases, whereas the content of —C=O apparently increases. It is possible that the Ag^+ adsorbs not only on the —C—OH sites but also on the surface of carbon fibers. And then the Ag^+ is reduced by —C—OH and carbon surface into Ag NPs, forming the oxygen-containing functional groups such as —C=O and —COOH.

As illustrated in Fig. 3e, two bands at 374.2 eV and 368.3 eV, ascribed to the typical Ag 3d5/2 and Ag3/2 binding energies [42,43], respectively, are observed. It suggests that the Ag species on the surface of CFs are the Ag NPs rather than Ag_2O or other species, conceding with the results of XRD patterns.
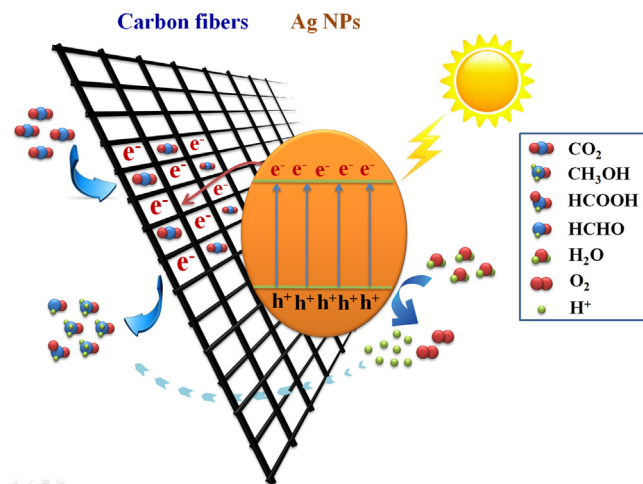
Scheme 1. Photocatalytic CO_2 reduction mechanisms of Ag NPs/CFs.

Overall, it can be obtained that the Ag NPs have been successfully prepared on the surface of CFs in the spherical shape. And the CFs not only act as the carrier but also the reducing reagent for the Ag^+ reduction. Amounts of polarized groups like —C=O and —COOH are formed on the surface of CFs after Ag^+ reduction.

3.2. Formation mechanisms

The mechanisms for the formation of Ag NPs/CFs are shown in Fig. 4a. Firstly, the Ag^+ generated from $AgNO_3$ is adsorbed on the surface of CFs. Comparable experiments were conducted with or without ultrasonic treatment in the preparation process to confirm the adsorption of Ag^+. The SEM images of the Ag NPs/CFs are shown in Fig. 4b and c as well as Fig. 2b and c. Compared to the ultrasonically treated samples, the untreated ones show irregular Ag NPs with nonuniform dispersion. It has been reported that ultrasonic treatment is a powerful method to disperse particles or ions. In the present study, the ultrasonic method makes some of the Ag^+ uniformly adsorbed on the surface of CFs including —C—OH and carbon surface (as shown in step 1 of Scheme 1).

Secondly, PVP was added into the above solutions and heated to 80 °C. The adsorbed and dissociative Ag^+ was reduced by both PVP and CFs (step 2). The precursor mixtures were analyzed by TEM analysis as shown in Fig. 4d and e. Black dots are observed in the solutions and on the surface of CFs, which are attributed to the Ag NPs [44,45], further indicating the reduction of Ag^+ by both PVP and CFs. In addition, it is possible that the ultrasonic treatment also results in the reduction of Ag^+. To confirm the Ag^+ reduction under the ultrasonic treatment, the Ag NPs/CFs was observed by SEM after ultrasonic treatment without adding PVP and heating. As shown in Fig. 4f and g, it can be seen that only a few Ag NPs are observed on the surface of CFs, indicating that the Ag^+ is also reduced by CFs during the ultrasonic treatment, but still mainly occurring in the heating process. Specifically, the Ag^+ tends more to be reduced on the defects of CFs as shown in Fig. 4g. The reduction of Ag^+ on the surface of CFs in $AgNO_3$ solution can benefit the aggregation of Ag NPs into spherical shape because such Ag NPs are able to act as the seeds for aggregation.
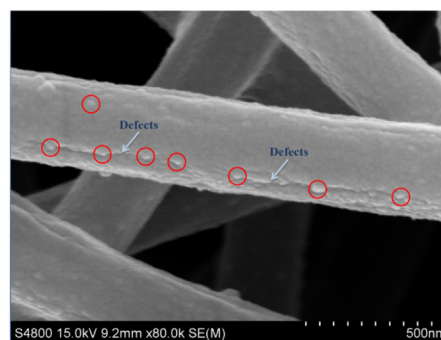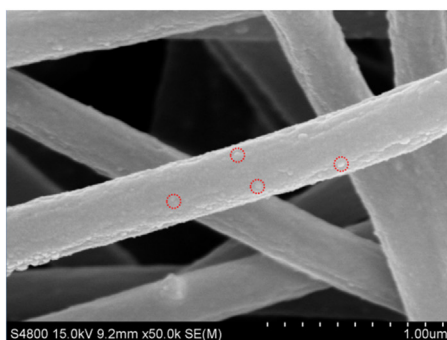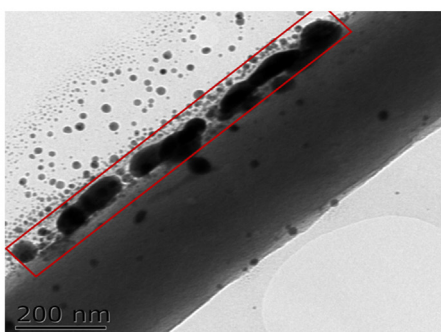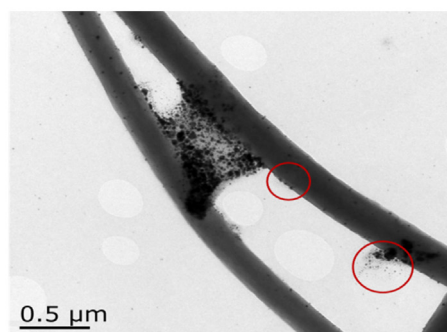
(a)

(b)

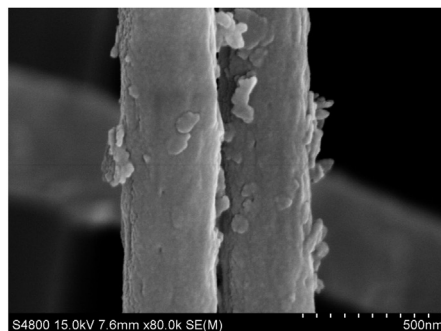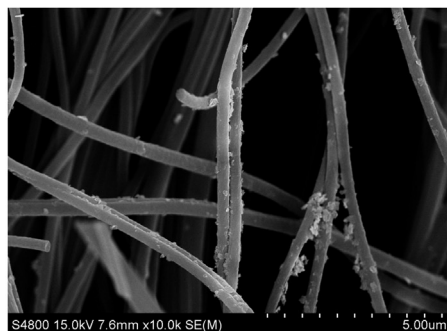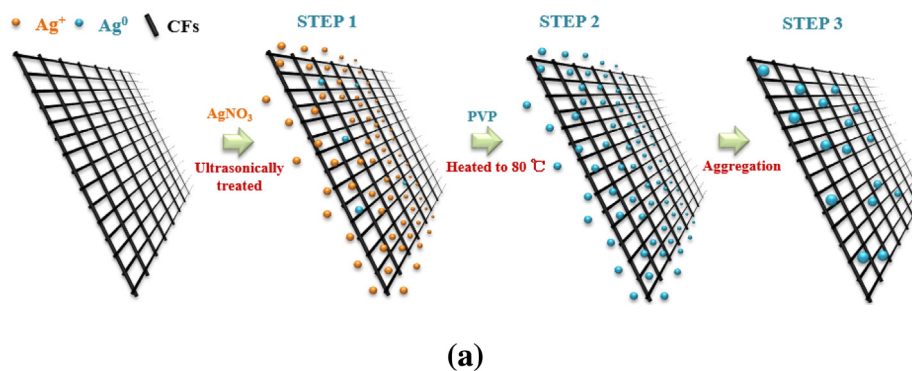
(c)

(d)

(e)

(f)

(g)

Fig. 4. Characteristics of catalyst formation. (a) Formation mechanisms of Ag NPs/CFs; (b,c) SEM images of Ag NPs/CFs without ultrasonic treatment; (d,e) TEM images of AgNO$_3$, PVP and CFs mixtures during ultrasonic treatment, (f,g) SEM images of Ag NPs/CFs with ultrasonic treatment without PVP adding and heating.

Finally, these Ag NPs reduced from Ag^+ are aggregated to form spherical Ag NPs on the surface of CFs through two ways (step 3): one is from solutions and the other is from the surface of CFs via Ostwald ripening. In the preparation process, the TEM characterizations of Ag NPs/CFs were conducted to analyze the formation mechanisms of spherical Ag NPs. As shown in the red circle area of Fig. 4d, the Ag NPs are apparently larger when the solution is rich in Ag NPs, indicating that the Ag NPs from the solution play an important role in the formation of spherical Ag NPs. As shown in Fig. 4e, the Ag NPs tend to be aggregated on the surface of CFs through Ostwald ripening. It suggests that the Ostwald ripening is also crucial to the formation of spherical Ag NPs.

Overall, such structural materials were formed through three steps: the adsorption of Ag^+ ions, the reduction of Ag^+ by both PVP and CFs, as well as the aggregation of Ag NPs to form spherical Ag NPs from the solutions and through Ostwald ripening.

3.3. Photocatalytic activity

To investigate the plasmonic photocatalytic activity of the Ag NPs/CFs, the photocatalytic reduction of CO_2 was carried out under visible light irradiation. The final products from CO_2 reduction over Ag NPs and Ag NPs/CFs were detected by gas chromatography (GC) (Fig. S3a). The results show that three kinds of species are detected by the GC-FID method for both Ag NPs and Ag NPs/CFs, with the CH_3OH predominant. And the other two species may be oxidized low-carbon organics like HCOOH and HCHO, which may be originated from the direct reduction of CO_2 or CH_3OH oxidation by oxidation species such as holes and O_2 produced in the catalytic reaction. As shown in the GC–MS spectra (Fig. S3b–e), low content of O_2 can be detected, indicating that the O_2 is generated in the reaction system. The CH_3OH in the gas phase is from the evaporation of the liquid products. These two productions are very low and can only be detected with GC–MS. The lower content of O_2 than the productions possibly support the oxidation of CH_3OH due to the O_2 consumption when oxidizing. Compared to Ag NPs, the Ag NPs/CFs tends to present higher selectivity of CH_3OH, which can be explained from three perspectives. Firstly, the photocatalytic reduction reaction could take place at the solid-gas interface. The oxidized low-carbon organic molecules such as HCOOH and HCHO are more likely to be adsorbed on the surfaces of catalysts than CH_3OH because of their stronger polarities. It was possible that only CH_3OH can be desorbed from the catalysts. Also, HCOOH and HCHO in higher oxidation states are relatively unstable molecules compared to CH_3OH, which can be readily re-oxidized into CO_2 by the oxidization species such as holes and O_2. More importantly, the active sites transfer from sole Ag NPs to both Ag NPs and CFs of Ag NPs/CFs for H_2O decomposition and CO_2 reduction, respectively, plays an important role in the selectivity of CH_3OH, because such transfer inhibits the oxidation of CH_3OH into oxidized low-carbon organic molecules including HCHO and HCOOH. Typically, when the CH_3OH is generated on the surface of CFs, the CH_3OH tends to become vapor at high temperature or dissolved in H_2O. The H_2O has higher polarity than CH_3OH and is more likely to be adsorbed on the Ag NPs. However, in the catalytic process with sole Ag NPs, the H_2O decomposition and CO_2 reduction are occurred on the same active sites. The holes and O_2 produced in the reaction may re-oxidize CH_3OH into HCOOH and HCHO and further convert them into CO_2, resulting in the low catalytic activity and selectivity. As described in Fig. S3a, the HCOOH and HCHO productions over Ag NPs compared to Ag NPs/CFs supports the transfer of active sites from sole Ag NPs to both Ag NPs and CFs. CH_3OH is one of the most desirable valuable fuels that are easy to be stored and utilized, while good selectivity of CH_3OH production can also effectively facilitate the subsequent product separation process.

Table 3
Comparison of CH_3OH production in the present study and previous reports.

Catalysts	CH_3OH production/ $(\mu g/mg\,h)$	Light source	Reference
Ag NPs/CFs	0.475	Visible	Present study
GO	4.960×10^{-3}	Solar	[46]
TiO_2	0.444	Ultraviolet	[48]
$BiVO_4$	0.133	Visible	[49]
AgX:Ag (X = Cl, Br)	0.090	Visible	[50]
WO_3 LDH1	1.800×10^{-3}	Visible	[51]
Ni@NiO/InTaO$_4$-N	0.150	Solar	[52]
NiO_X-Ta_2O_5-rG	0.400	Ultraviolet	[53]
Bi_2WO_6	0.075	Solar	[54]
Zn-Cu-Ga	3.200×10^{-3}	visible	[55]
GO-$CS_2Mo_6Br_8{}^1Br_X$[a]	0.064	Visible	[56]

Fig. 5 presents the comparison of CH_3OH production over CFs, Ag NPs and Ag NPs/CFs calculated from the GC spectra based on the integral area between each peak and baseline. About 3.5 μg CH_3OH can be produced after 5 h reaction over Ag NPs due to its production of surface Plasmon resonance electrons under the visible light. Interestingly, much higher CH_3OH production, as high as 12.5 μg CH_3OH, can be detected over Ag NPs/CFs. Because the oxidized low-carbon organics like HCOOH and HCHO are extremely low over Ag NPs and Ag NPs/CFs, they are difficult to be accurately calculated. It is interesting that the CH_3OH production increased dramatically in the initial time, while it becomes much slow with the time. This phenomenon has also been reported by others over graphene oxide and Cu/TiO_2 photocatalysts [46,47], and the maximum production of CH_3OH reached the highest values within 2 h. It is possible that both H_2O and produced CH_3OH can act as reduction agent in the photocatalytic reactions. In the initial time, the H_2O mainly acts as the reduction agent due to the low CH_3OH concentration. When the CH_3OH concentration reaches a certain value, the consumption of CH_3OH becomes large, which negatively affected CH_3OH production. The exhaust gases have also been detected in the present study. No organic products were detected. It indicates that there are no gaseous organic products or generated in this process under the detection limit of GC.

To confirm the carbon source in the CH_3OH is from CO_2, a ^{13}C-labled isotopic experiment by using $^{13}CO_2$ instead of the standard CO_2 was carried out, and the produced CH_3OH was analyzed by GC–MS. Fig. 5b shows the results of the GC–MS analysis. The mass spectrum of the peak attributed to $^{13}CH_3OH$ is different from that of standard CH_3OH, i.e., m/z values are larger in the $^{13}CH_3OH$ by 1 unit. Under the $^{13}CO_2$ atmosphere, the Ag NPs/CFs and H_2O mixture were irradiated. The GC–MS analysis shows the formation of $^{13}CH_3OH$ from the photochemical reaction. However, when the standard CO_2 is used, the $^{13}CH_3OH$ is hardly detected while the standard CH_3OH is clearly distinguishable. It indicates that the carbon in photochemical produced CH_3OH almost entirely originated from CO_2.

As exhibited in Table 3, CH_3OH production in the present study is compared to those reported in the previous literatures to prove the well catalytic activities of Ag NPs/CFs. CH_3OH production in the present study is higher than those in previous reports.

3.4. Possible photocatalytic mechanisms

The enhanced plasmonic photocatalytic activity of Ag NPs/CFs may be ascribed to the well dispersion of Ag NPs on the surface of CFs, the efficient charge transfer and separation as well as the high CO_2 adsorption. The effect of wavelength on the catalytic activities of CFs, Ag NPs and Ag NPs/CFs are shown in Fig. S4. It can be seen that the catalytic activity of Ag NPs/CFs slightly decreases with the wavelength, while the one of Ag NPs decreases notably. This indi-
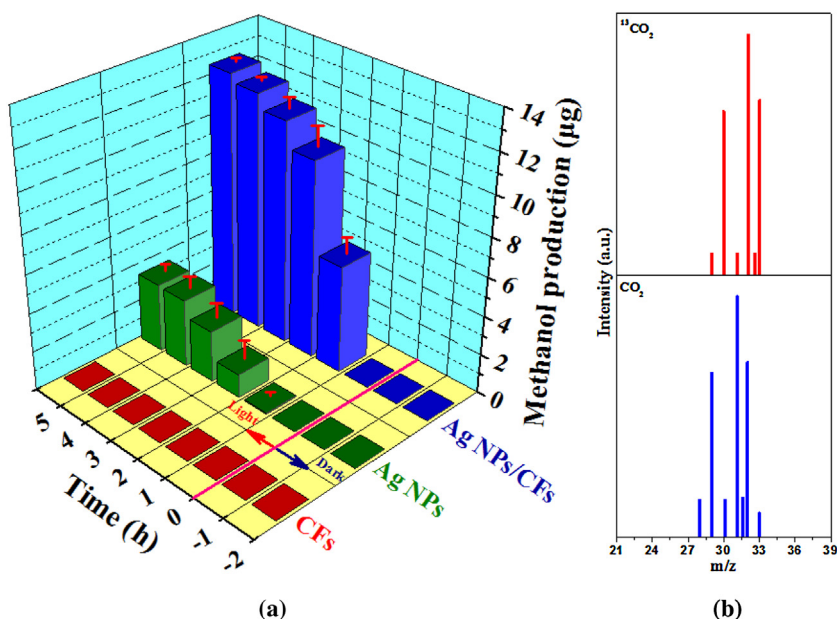
Fig. 5. Results of photocatalytic reduction of CO_2. (a) Comparison of photocatalytic CH_3OH production of CFs, Ag NPs and Ag NPs/CFs; (b) Isotope experiment of photocatalytic CO_2 reduction.

cates that the catalytic activities of Ag NPs and Ag NPs/CFs depend much on the characteristics of light sources. A possible mechanism is proposed to explain the better performance of Ag NPs/CFs catalytic system. It has been reported that, in some metals like Ag and Au, the electrons were able to be photoexcited from HOMO to LUMO under visible light irradiation to produce Plasmon-excited electrons and electron-hole pairs [12,57]. When the Ag NPs/CFs are subjected to the visible light irradiation, the well dispersion of Ag NPs promotes the light absorption and generates more Plasmon-excited electrons on the surface of Ag NPs and thereby enhances the photocatalytic reduction of CO_2. These Plasmon-excited electrons transfer to the CFs by the interface between Ag NPs and CFs or some linkage bonds, thus inhibiting the electron-hole recombination and promoting the photocatalytic activity. In previous studies, the coverage of Ag NPs on the carbon-based materials were also reported, and the oxidation-reduction reactions occurred including the present study during the catalyst preparation [27]. Such oxidation-reduction reactions easily lead to the formation of some linkage bonds between Ag NPs and CFs. In the present study, no linkage bonds have been formed during the preparation process even though parts of Ag^+ adsorb on the C—OH in the initial step, according to FTIR and XPS analyses. Therefore, the Plasmon-excited electrons on the Ag NPs transfer to the CFs only through the interface between Ag NPs and CFs. After the electrons transfer from Ag NPs to CFs, the remaining holes represented with h^+ in the Ag NPs decomposes H_2O into H^+ and O_2 as follows [10,58]:

$$2H_2O + 4h^+ \rightarrow 4H^+ + O_2 \quad (1)$$
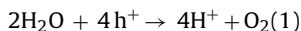
The noble metal nanoparticles including Ag NPs have been reported to show strong reactivity with H_2O [10,58] and the O_2 has been detected by GC–MS (Fig. S3b–e), further confirming the reaction (1). It is possible that the O_2 generated in the reaction system oxidize the Ag NPs into Ag_2O, resulting in the inactivation of Ag NPs. The fresh and used Ag NPs/CFs were measured by XRD patterns and XPS spectra as shown in Fig. S5. XRD results show that the Ag NPs/CFs hardly exhibit any changes after reaction, indicating the stability of Ag NPs/CFs and without any generation of Ag_2O during the reaction process. The Ag 3d XPS spectra show that there are two peaks at 374.2 eV and 368.3 eV corresponding to metallic Ag,

indicating that the main silver species are still the metallic silver in the used Ag NPs/CFs. The SEM images of used Ag NPs/CFs illustrate no apparent aggregations of silver, further confirming the stability of the catalysts (Fig. S6).

More importantly, the photocatalytic reaction also involves the transportation of CO_2 molecule over the catalyst surface. The CO_2 can be adsorbed and concentrated on the surface of CFs due to the high CO_2 adsorption capacity of CFs. Under visible light irradiation, the concentrated CO_2 molecules over catalyst surface accelerate them to obtain the electrons from CFs generated by Ag NPs, thus resulting in the faster reduction of CO_2, promoting the photocatalytic reduction toward CO_2 molecules. The hydrogen in CH_3OH is from the H^+ generated by the decomposition of H_2O on Ag NPs sites as the following equations [57,59]:

$$CO_2 + 6H^+ + 6e^- \rightarrow CH_3OH + H_2O \quad (2)$$
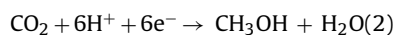
In the above possible mechanism, the CFs and Ag NPs in the Ag NPs/CFs are responsible for the CO_2 photoreduction and H_2O decomposition, respectively, supported by the results of in part 3.3. The overall mechanisms are shown in Scheme 1. In this process, the O_2 generated may oxidize the CH_3OH productions and inhibit the CO_2 reduction. However, the O_2 generation and CO_2 reduction are occurred in separate sites, and the O_2 is only a little soluble in H_2O. Both inhibit the oxidation of CH_3OH productions and promote the reduction of CO_2.

3.5. Optical, electrochemical and adsorption characterizations

To confirm the enhancement of photocatalytic reduction of CO_2 as well as the above possible mechanisms, optical, electrochemical and adsorption characterizations have been conducted. Fig. 6a displays the UV–vis absorption spectra of Ag NPs, CFs and Ag NPs/CFs. It can be seen that the Ag NPs/CFs exhibits the strongest absorption in the visible light region (400–800 nm), indicating that the well dispersion of Ag NPs promotes the light absorption. The intensive absorption in visible light region of the Ag NPs/CFs possibly means the enhanced adsorption for the photoreduction of CO_2 and thereby presents higher activity in the photocatalysis than CFs and
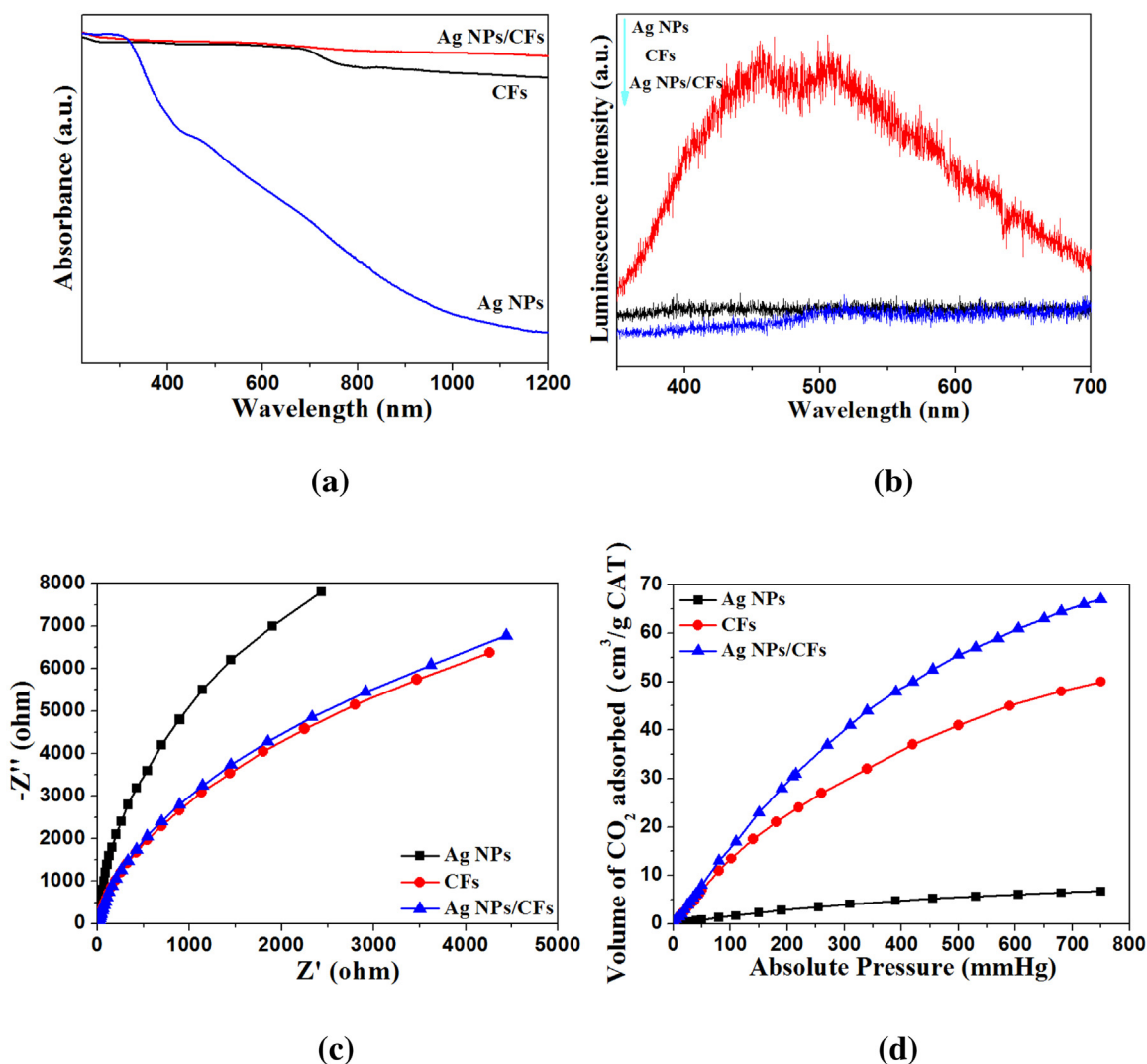
Fig. 6. UV–vis diffuse-reflectance spectra (a); photoluminescence spectra (b); EIS Nyquist plots (c); CO_2 adsorption curves (d).

Ag NPs. Compared to Ag NPs, the CFs show much higher absorption, possibly due to the black color of CFs [34].

The measured PL-emission spectra of Ag NPs, CFs and Ag NPs/CFs in the range of 350–700 nm are illustrated in Fig. 6b. An apparent peak can be observed for Ag NPs, being similar with previous papers reported [60,61], indicating that the electrons can be excited by irradiation in Ag NPs. Compared to the Ag NPs, the intensity of the PL spectra dramatically decreases for Ag NPs/CFs, while the CFs exhibits no PL emission, conceding with the literature [62].The reduction of the PL-intensity indicates the diminution of the electron/hole pairs recombination process [63,64]. Therefore, in the Ag NPs/CFs, the CFs can significantly inhibit the recombination of light-induced electrons and holes, thus resulting in high photocatalytic activities. This could result from the electron transfer from Ag NPs to CFs, as indicated in the above mentioned mechanisms, thus promoting the separation of electrons and holes. Interestingly, although CFs exhibit high adsorption of visible light and low PL peak intensity, they hardly exhibit any photoredcution of CO_2. As is known, CFs cannot produce any electrons to reduce CO_2 under the visible light even though it exhibits well adsorption of CO_2, indicating the critical role of Ag NPs in the photocatalytic reaction system.

EIS is a powerful technique for examining the separation efficiency of the photogenerated electron-holes and charge trans-

fer resistance across the surface of photoelectrodes [65]. Fig. 6c presents the Nyquist impedance spectra of the Ag NPs, CFs, and Ag NPs/CFs. In general, a smaller arc radius in the EIS plot indicates a smaller electron transfer resistance at the surface of the photoelectrodes, which normally leads to more effective separation of the photoelectron-hole pairs and faster interfacial charge transfer [66]. The Ag NPs show much larger semicircular arc compared to the CFs, indicating less electron transfer resistance of CFs, which suggests that the electrons can be successfully transferred from Ag NPs to CFs. It is the basis of the possible mechanisms of active site splitting in the present study, which requires the oxidation and reduction occurring on different active sites. When the electrons are successfully transferred from Ag NPs to CFs, the h$^+$ remaining in the Ag NPs may decompose H_2O, and the electron-rich CFs may reduce CO_2. The surface modification of Ag on the semiconductors has been widely reported [67–69]. The Ag modifications were able to apparently decrease the electron transfer resistance of semiconductors. However, being different from previous reports, the electron resistance slightly increases after the Ag NPs modification on the CFs, which may be ascribed to the conductor property of CFs (not semiconductor) and the increase in defects on the surface of CFs by modification of Ag NPs [70,71]. And the defects can capture electrons and enhance the electron transfer resistance. Moreover, the lower semicircular arc of Ag NPs/CFs compared to Ag NPs indi-

Table 4
BET surface areas, pore sizes and pore volumes of Ag NPs, CFs and Ag NPs/CFs.

Samples	Surface areas (m^2/g)	Pore diameters (nm)	Pore volumes ($cm^3\,g^{-1}$)
Ag NPs	102.72	34.04	10.20
CFs	497.72	30.60	60.31
Ag NPs/CFs	352.69	30.62	30.20

cates faster interfacial charge transfer and better separation of the photogenerated electron-hole pairs under visible light irradiation. It further indicates that the CFs promote the electron transfer and charge separation of Ag NPs, resulting in the higher reduction of CO_2.

As shown in Fig. 6d, both CFs and Ag NPs/CFs show well adsorption capacity for CO_2, reaching up to 50 and 67 cm^3/g catalysts at 750 mmHg, conceding with the results reported [72,73]. The Ag NPs show much lower adsorption capacity. It may be caused by the larger surface areas of Ag NPs/CFs compared to Ag NPs as shown in Fig. S7 and Table 4. The strong CO_2 adsorption on CFs proves the CO_2 photoreduction over CFs as the above mentioned and further supports the possible mechanisms of active site splitting. The Ag NPs/CFs exhibits a more excellent adsorption capacity than CFs, maybe due to the rough surface of Ag NPs/CFs including amounts of polar groups like —C=O, —COOH. The adsorption of CO_2 on the surface of CFs facilitates the electrons transfer from CFs to the CO_2, resulting in the higher reduction of CO_2.

4. Conclusions

Ag NPs/CFs plasmonic photocatalysts with high activity have been successfully synthesized through a solution dipping and ultrasonic treatment. The photocatalytic reduction of CO_2 with CFs, Ag NPs and Ag NPs/CFs is conducted under the visible light irradiation. Some low-carbon organics are produced with CH_3OH predominated. With unique structures, Ag NPs/CFs shows up to 4-fold enhancement of CH_3OH in CO_2 photoreduction than Ag NPs toward CO_2 reduction. The well dispersion of Ag NPs, the enhanced charge separation and the well adsorption of CO_2 as well as the splitting of active sites from sole Ag NPs to both Ag NPs and CFs are responsible for the significant enhancements. This study will motivate new developments in plasmonic photocatalyst methodology and promote their practical application in environmental issues.

Acknowledgements

Appendix A. Supplementary data

Supplementary data associated with this article can be found, in the online version, at http://dx.doi.org/10.1016/j.apcatb.2016.09.038.

References

[1] S. Wang, X. Wang, Angew. Chem. Int. Ed. 55 (2016) 2308–2320.
[2] S. Wang, X. Wang, Multifunctional metal-organic frameworks for photocatalysis, Small 11 (2015) 3097–3112.
[3] S. Neatu, J.A. Macia-Agullo, P. Concepcion, H. Garcia, J. Am. Chem. Soc. 136 (2014) 15969–15976.
[4] Y. He, Y. Wang, L. Zhang, B. Teng, M. Fan, Appl. Catal. B: Environ. 168 (2015) 1–8.
[5] T. Inoue, A. Fujishima, S. Konishi, K. Honda, Nature 277 (1979) 637–638.
[6] S. Wang, Z. Ding, X. Wang, Chem. Commun. 51 (2015) 1517–1519.
[7] S. Wang, W. Yao, J. Lin, Z. Ding, X. Wang, Angew. Chem. Int. Ed. 53 (2014) 1034–1038.
[8] L. Liu, H. Zhao, J.M. Andino, Y. Li, ACS Catal. 2 (2012) 1817–1828.
[9] S.N. Habisreutinger, L. Schmidt-Mende, J.K. Stolarczyk, Angew. Chem. Int. Ed. 52 (2013) 7372–7408.
[10] S. Sato, T. Arai, T. Morikawa, K. Uemura, T.M. Suzuki, H. Tanaka, T. Kajino, J. Am. Chem. Soc. 133 (2011) 15240–15243.
[11] S. Xie, Y. Wang, Q. Zhang, W. Fan, W. Deng, Y. Wang, Chem. Commun. 48 (2013) 2451–2453.
[12] H. Zhang, X. Fan, X. Quan, S. Chen, H. Yu, Environ. Sci. Technol. 45 (2011) 5731–5736.
[13] X. Ma, Y. Dai, L. Yu, Z. Lou, B. Huang, M.H. Whangbo, J. Phys. Chem. C 118 (2014) 12133–12140.
[14] H. Lim, H. Shim, W.A. Goddard, Y.J. Hwang, B.K. Min, H. Kim, J. Am. Chem. Soc. 126 (2014) 11355–11361.
[15] Y. He, L. Zhang, B. Teng, M. Fan, Environ. Sci. Technol. 49 (2015) 649–656.
[16] M. Yamamoto, T. Yoshida, N. Yamamoto, T. Nomoto, Y. Yamamoto, S. Yagi, H. Yoshida, J. Mater. Chem. A 3 (2015) 16810–16816.
[17] M. Endo, Y.A. Kim, T. Hayashi, K. Nishimura, T. Matusita, K. Miyashita, M.S. Dresselhaus, Carbon 39 (2001) 1287–1297.
[18] L. Wang, Y. Yao, Z. Zhang, L. Sun, W. Lu, W. Chen, H. Chen, Chem. Eng. J. 251 (2014) 348–354.
[19] P. Kung, L. Huang, T. Shen, W. Wang, Y. Su, M.I. Lei, Appl. Phys. Lett. 106 (2015) 023114-1–023114-5.
[20] E. Stratakis, M.M. Stylianakis, E. Koudoumas, E. Kymakis, Nanoscale 5 (2013) 4144–4150.
[21] E. Thimsen, F.L. Formal, M. Cratzel, S.C. Warren, Nanoletters 11 (2011) 35–43.
[22] X.Y. Ling, R. Yan, S. Lo, D.T. Hoang, C. Liu, M.A. Fardy, S.B. Khan, A.M. Asirin, S.M. Bawaked, P. Yang, Nano Res. 7 (2014) 132–143.
[23] J. Tian, S. Liu, Y. Zhang, H. Li, L. Wang, Y. Luo, A.M. Asiri, A.O. Al-Youbi, X. Sun, Inorg. Chem. 51 (2012) 4742–4746.
[24] T. Wu, S. Liu, Y. Luo, W. Lu, L. Wang, X. Sun, Nanoscale 3 (2011) 2142–2144.
[25] S. Wang, Y. Hou, X. Wang, ACS Appl. Mater. Interfaces 7 (2015) 4327–4335.
[26] S. Mondal, U. Rana, S. Malik, ACS Appl. Mater. Interfaces 7 (2015) 10457–10465.
[27] M. Sawangphruk, M. Suksomboon, K. Kongsupornsak, J. Khuntilo, P. Srimuk, Y. Sanguansak, P. Klunbud, P. Suktha, P. Chiochan, J. Mater. Chem. A 1 (2013) 9630–9636.
[28] N.R. Srinivasan, P.A. Shankar, R. Bandyopadhyaya, Carbon 57 (2013) 1–10.
[29] S. Biniak, G. Szymanski, J. Siedlewski, A. Swiatkowski, Carbon 35 (1997) 1799–1810.
[30] H. Ortiz, N. Casillas, V. Soto, M. Barcena-Soto, R. Torres-Vitela, W. de la Cruz, S. Gomez-Salazar, J. Colloid Interface Sci. 314 (2007) 562–571.
[31] X. Song, P. Gunawan, R. Jiang, S.S.J. Leong, K. Wang, R. Xu, J. Hazard. Mater. 194 (2011) 162–168.
[32] S. Gamburzev, K. Petrov, A.J. Appleby, J. Appl. Electrochem. 32 (2002) 805–809.
[33] V.J. González, E. Gracia-Espino, A. Morelos-Gómez, F. López-Urías, H. Terrones, M. Terrones, Carbon 88 (2015) 51–59.
[34] A.B. Castle, E. Gracia-Espino, C. Nieto-Delgado, H. Terrones, M. Terrones, S. Hussain, ACS Nano 5 (2011) 2458–2466.
[35] K.A.S. Fernando, V.G. Watson, X. Wang, N.D. McNamara, M.C. JoChum, D.W. Bair, B.A. Miller, C.E. Bunker, Langmuir 30 (2014) 11776–11784.
[36] M. Zheng, Y. Liu, K. Jiang, Y. Xiao, D. Yuan, Carbon 48 (2010) 1224–1233.
[37] N. Díez, P. Alvarez, M. Granda, C. Blanco, R. Santamaría, R. Menéndez, Chem. Eng. J. 260 (2015) 463–468.
[38] M.S. Islam, Y. Deng, L. Tong, S.N. Faisal, A.K. Roy, A.I. Minett, V.G. Gomes, Carbon 96 (2016) 701–710.
[39] Y. Yao, L. Wang, L. Sun, S. Zhu, Z. Huang, Y. Mao, W. Lu, W. Chen, Chem. Eng. Sci. 101 (2013) 424–431.
[40] M.E. Eberhart, M.J. Donovan, R.A. Outlaw, Phys. Rev. B 46 (1992) 12744–12747.
[41] L. Pei, J. Zhou, L. Zhang, Build. Environ. 63 (2013) 108–113.
[42] M. Zhu, P. Chen, M. Liu, ACS Nano 5 (2011) 4529–4536.
[43] Y. Yang, Y. Guo, F. Liu, X. Yuan, Y. Guo, S. Zhang, W. Guo, M. Huo, Appl. Catal. B: Environ. 142–143 (2013) 828–837.
[44] N.G. Bastus, F. Merkoci, J. Piella, V. Puntes, Chem. Mater. 26 (2014) 2836–2846.

[45] J. Lin, J. Cui, F. Vilela, J. He, M. Zeller, A.D. Hunter, Z. Xu, Chem. Commun. 51 (2015) 12197–12200.

[46] H. Hsu, I. Shown, H. Wei, Y. Chang, H. Du, Y. Lin, C. Tseng, C. Wang, L. Chen, Y. Lin, K. Chen, Nanoscale 5 (2013) 262–268.

[47] Y. Li, W. Wang, Z. Zhan, M. Woo, C. Wu, P. Biswas, Appl. Catal. B: Environ. 100 (2010) 386–392.

[48] J. Wang, H. Liu, Y. Xu, X. Zhang, Asian J. Chem. 26 (2014) 3875–3878.

[49] J. Mao, T. Peng, X. Zhang, K. Li, L. Zan, Catal. Commun. 28 (2012) 38–41.

[50] C. An, J. Wang, W. Jiang, M. Zhang, X. Ming, S. Wang, Q. Zhang, Nanoscale 4 (2012) 5646–5650.

[51] M. Morikawa, Y. Ogura, N. Ahmed, S. Kawamura, S. Okamoto, Y. Izumi, Catal. Sci. Technol. 4 (2014) 1644–1651.

[52] C. Tsai, H.M. Chen, R. Liu, K. Asakura, T. Chan, J. Phys. Chem. C 115 (2011) 10180–10186.

[53] X. Lv, W. Fu, C. Hu, Y. Chen, W. Zhou, RSC Adv. 3 (2013) 1753–1757.

[54] L. Liang, F. Lei, S. Gao, Y. Sun, X. Jiao, J. Wu, S. Qamar, Y. Xie, Angew. Chem. Int. Ed. 54 (2015) 13971–13974.

[55] N. Ahmed, Y. Shibata, T. Taniguchi, Y. Izumi, J. Catal. 279 (2011) 123–135.

[56] P. Kumar, H.P. Mungse, S. Cordier, R. Boukherroub, O.P. Khatri, S.L. Jain, Carbon 94 (2015) 91–100.

[57] F. Xiao, Z. Zeng, B. Liu, J. Am. Chem. Soc. 137 (2015) 10735–10744.

[58] T. Arai, S. Sato, T. Kajino, T. Morikawa, Energy Environ. Sci. 6 (2013) 1274–1282.

[59] H. Hsu, I. Shown, H. Wei, Y. Chang, H. Du, Y. Lin, C. Wang, L. Chen, Y. Lin, K. Chen, Nanoscale 5 (2013) 262–268.

[60] Y. Zhao, Y. Jiang, Y. Fang, Spectrochim. Acta A 65 (2006) 1003–1006.

[61] A. Alqudami, S. Annapoorni, Plasmonics 2 (2007) 5–13.

[62] Y.H. Ko, D.K.V. Ramana, J.S. Yu, Nano Res. Lett. 8 (2013) 262–269.

[63] S. Wang, X. Wang, Appl. Catal. B: Environ. 162 (2015) 494–500.

[64] S. Wang, J. Lin, X. Wang, Phys. Chem. Chem. Phys. 16 (2014) 14656–14660.

[65] J. Gan, X. Lu, J. Wu, S. Xie, T. Zhai, M. Yu, Z. Zhang, Y. Mao, S.C. Wang, Y. Shen, Y. Tong, Sci. Rep. 3 (2013) 1021–1028.

[66] J. Li, L. Liu, Y. Yu, Y. Yu, Y. Tang, H. Li, F. Du, Electrochem. Commun. 6 (2004) 940–943.

[67] S. Liu, B. Weng, Z.T. Tang, Y.J. Xu, Nanscale 7 (2015) 861–866.

[68] Z. Chen, L. Fang, W. Dong, F. Zheng, M. Shen, J. Wang, J. Mater. Chem. A 2 (2014) 824–832.

[69] M. Ayan-Varela, M.J. Fernandez-Merino, J.I. Paredes, S. Villar-Rodil, C. Fernandez-Sanchez, L. Guardia, A. Martinez-Alonson, J.M.D. Tascon, J. Mater. Chem. A 2 (2014) 7295–7305.

[70] S.A. Ansari, M.M. Khan, M.O. Ansari, M.H. Cho, Sol. Energy Mater. Sol. Cells 141 (2015) 162–170.

[71] S. Kuo, W. Tuan, J. Shieh, S. Wang, J. Eur. Ceram. Soc. 27 (2007) 4521–4527.

[72] S. Lee, S. Park, J. Colloid Interface Sci. 389 (2013) 230–235.

[73] D. Cazorla-Amoros, J. Alcaniz-Monge, A. Linares-Solano, Langmuir 12 (1996) 2820–2824.